Nanoparticle amount, and not size, determines chain alignment and nonlinear hardening in polymer nanocomposites

H. Samet Varol[a], Fanlong Meng[b], Babak Hosseinkhani[c], Christian Malm[a], Daniel Bonn[d], Mischa Bonn[a], Alessio Zaccone[b,e], and Sapun H. Parekh[a,1]

[a]Department of Molecular Spectroscopy, Max Planck Institute for Polymer Research, 55128 Mainz, Germany; [b]Cavendish Laboratory, University of Cambridge, Cambridge CB3 0HE, United Kingdom; [c]SKF Engineering & Research Center, 3430DT Nieuwegein, The Netherlands; [d]Institute of Physics, University of Amsterdam, 1098 XH Amsterdam, The Netherlands; and [e]Department of Chemical Engineering and Biotechnology, University of Cambridge, Cambridge CB2 3RA, United Kingdom

Edited by David A. Weitz, Harvard University, Cambridge, MA, and approved February 28, 2017 (received for review October 14, 2016)

Polymer nanocomposites—materials in which a polymer matrix is blended with nanoparticles (or fillers)—strengthen under sufficiently large strains. Such strain hardening is critical to their function, especially for materials that bear large cyclic loads such as car tires or bearing sealants. Although the reinforcement (i.e., the increase in the linear elasticity) by the addition of filler particles is phenomenologically understood, considerably less is known about strain hardening (the nonlinear elasticity). Here, we elucidate the molecular origin of strain hardening using uniaxial tensile loading, microspectroscopy of polymer chain alignment, and theory. The strain-hardening behavior and chain alignment are found to depend on the volume fraction, but not on the size of nanofillers. This contrasts with reinforcement, which depends on both volume fraction and size of nanofillers, potentially allowing linear and nonlinear elasticity of nanocomposites to be tuned independently.

nanocomposites | nonlinear elasticity | strain stiffening | polymer bridging | polymer chain alignment

Many synthetic and natural materials around us increase their elastic modulus upon large deformation after initial softening—a phenomenon that is known as work or strain hardening, which is critical to their function. In ductile polymer materials, the strain-hardening behavior is essential for their functional lifetime, resilience, and toughness—all key parameters of their practical uses—because these materials repetitively bear large loads (1, 2). Many industrial and consumer polymeric materials are composites, in which (hard) nanoscale inorganic particles, or fillers, are blended with polymer matrices to tailor their mechanical properties. In preparing such nanocomposites, filler–filler and filler–matrix interaction, filler dispersion, and polymer properties all affect the linear (low strain) and nonlinear (high strain) mechanical response in nontrivial ways (3). Although a massive volume of work has attempted to clarify the mechanism of reinforcement (increased linear elasticity) at low strain and of nonlinear strain softening (the Payne and Mullins effects) at medium strain, a comparatively much smaller body of work exists that focuses on the mechanism of strain hardening in polymer composite materials.

In analogy to rubber elasticity at large deformations, strain hardening in polymer composites is typically attributed to the increasing resistance to deformation of extended and oriented polymer chains (4–7). However, it has been shown that polymer chain alignment during strain hardening is strongly affected by dispersing fillers within the host polymer matrix (8–10). To account for these observations, one needs to establish the relation between the macroscopically observed strain hardening and the microscopic chain alignment that is affected by the presence of fillers.

The connection between chain alignment and strain hardening in glassy polymer composites is purported to occur because the fillers act as "entanglement attractors." In this picture, the segmental mobility of the polymer is disturbed (e.g., strongly constrained) by the presence of a large amount of surface area of the nanofillers, causing an increase in the number of physical entanglements; this results in greater alignment of effectively shorter segments between entanglement points in response to the applied load (8, 11). Consistent with this idea, Jancar et al. (8) showed that encapsulating micrometer-sized fillers in poly (methyl methacrylate) (PMMA) had negligible effect on the strain-hardening properties of the PMMA matrix as opposed to the inclusion of the same volume fraction of nanofillers, which induced substantial strain hardening. This finding suggests a clear role for both filler size and amount in strain hardening. Indeed, a similar idea—fillers acting as entanglement attractors—was proposed in 2002 by Sternstein and Zhu (12) as to the reason for augmented reinforcement as filler size decreases. However, because of the high glass transition temperature (T_g) for PMMA, simultaneous measurement of chain alignment was not possible in these experiments. Measuring chain alignment as a function of deformation in real time is possible in elastomer-based nanocomposites, which have a T_g well below room temperature. This characteristic allows investigation of the effect of nanofiller size and volume fraction on strain hardening and chain alignment simultaneously; previous studies have focused

Significance

When straining materials (e.g., pulling a rubber band), they initially deform with a certain stiffness; if one pulls harder, some materials strengthen. This phenomenon, known as nonlinear strain hardening, is a critical feature of composite polymer materials—polymers with reinforcing filler particles—used in, e.g., car tires. Engineering properties such as modulus, toughness, and strength of nanocomposites have been traditionally optimized through trial and error by changing the size and amount of fillers. Our work elucidates the molecular origin of strain hardening in polymer nanocomposites, showing that filler amount, but not size, sets the strain-hardening properties based on interfiller chain elongation. The insensitivity to filler size provides a facile concept to independently tune linear and nonlinear mechanics in composites.

Author contributions: H.S.V. and S.H.P. designed research; H.S.V., F.M., C.M., and A.Z. performed research; B.H., M.B., and S.H.P. contributed new reagents/analytic tools; H.S.V., F.M., D.B., M.B., A.Z., and S.H.P. analyzed data; and H.S.V., F.M., C.M., D.B., M.B., A.Z., and S.H.P. wrote the paper.

The authors declare no conflict of interest.

This article is a PNAS Direct Submission.

[1]To whom correspondence should be addressed. Email: parekh@mpip-mainz.mpg.de.

This article contains supporting information online at www.pnas.org/lookup/suppl/doi:10.1073/pnas.1617069114/-/DCSupplemental.

on either mechanical strain hardening (13–16) or chain alignment (17–20), but not both.

We investigate the strain-hardening mechanics and chain alignment in cross-linked, uniaxially loaded acrylonitrile butadiene rubber (NBR) nanocomposites ($T_g \approx -30$ °C) containing different amounts and sizes of SiO_2 nanofillers. Filler aggregate dispersion in different composites was quantified using transmission electron microscopy (TEM). Strain hardening was quantified by the increase in neo-Hookean (Gaussian) modulus (G_p), extracted from uniaxial tensile tests (21, 22). Combined with polarized Raman microspectroscopy measurements of chain alignment during uniaxial deformation, we find that the increase in G_p is directly proportional to chain alignment, and both depend on filler volume fraction but are surprisingly independent of filler size and morphology. Using simple scaling arguments, we show that the observed chain alignment is dominated by "bridging" chains between filler aggregates. We find that chain alignment is independent of filler size because of a coupling between interfiller spacing (related to bridging chain alignment) and volume fraction of fillers (related to total amount of bridging chains that become aligned). This finding demonstrates a clear distinction between the origin of nonlinear strain hardening (for which we find the nanofiller size to be irrelevant) and linear reinforcement (for which nanofiller size is important) (12, 23) for elastomer nanocomposite materials.

Results and Discussion

Nanocomposite Morphology. It was shown previously that the linear viscoelastic properties (reinforcement) of elastomer composite materials scaled with both the amount and size of dispersed nanofillers and microfillers for numerous elastomer polymer composites (23). Here, we focus on elastomer nanocomposites made from NBR (M_w = 250,000 g/mol) loaded with various amounts (quantified as the volume fraction, Φ) and sizes (D_p) of silica (SiO_2) nanofillers. The nanocomposites are produced by melt processing and mixing (*Materials and Methods*). Fig. 1*A* shows the basic formulation of the nanocomposites studied here, which contain NBR (green) and one of the two different primary particle-sized (D_p) fillers (blue). All nanocomposites are vulcanized (cross-linked) (Fig. 1*A*, black dotted lines). Importantly, no additional coating or coupling agents are used in these composites to modulate filler–NBR interaction, so the composite system is as simple as possible. This was emphasized by examination of all formulations by Fourier transform infrared spectroscopy, which showed no detectable hydrogen bonding or chemical interaction between the fillers and NBR chains (*SI Appendix*, Fig. S1) (24, 25); this strongly suggests that NBR chains interact with silica fillers via relatively weak van der Waals interactions (see *SI Appendix* for detailed estimation of interaction strength).

Fig. 1*B* shows TEM images of ultracryotomed sections of the four different nanocomposite formulations studied in this work. Light and dark contrast regions in micrographs show the elastomeric matrix and silica aggregates, respectively. Image analysis of TEM micrographs was used to quantify the filler aggregate size (R_{agg}) and dispersion (26). Aggregate outlines are depicted by red borders in each micrograph shown in Fig. 1*B*. From left to right, composites contain increasing Φ, with Φ = 3%, 14%, and 22.5%, respectively. The two images with Φ = 14% contain different D_p (15 nm and 28 nm) silica, whereas all other images contain D_p = 15 nm. Histograms of all detected aggregates from each nanocomposite are shown in *SI Appendix*, Fig. S2. Because a normal (Gaussian) distribution does not accurately fit these histograms, we used a weighted average over the histogram for those events that comprised 90% of the detected aggregate areas to calculate a mean aggregate size, R_{agg} (*Materials and Methods*); this

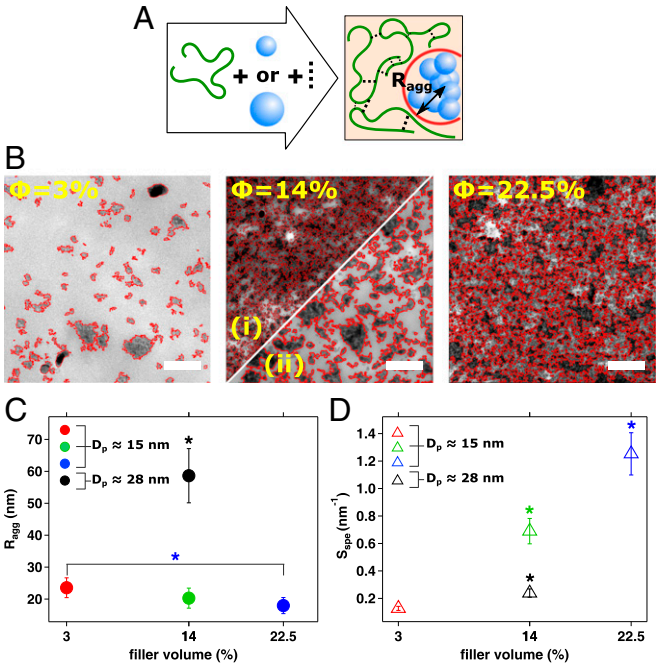

Fig. 1. Formulation and ultrastructural characterization of nanocomposite materials. (*A*) Main ingredients and final microstructure of the SiO_2/NBR nanocomposites. Green curved line and black dashed line represent NBR molecule and sulfur cross-links, respectively. The two different-sized blue balls represent the small- and large-size nanofillers. (*B*) TEM images after image analysis of SiO_2/NBR composites with different volume fraction (Φ) and primary particle size (D_p) of fillers; *i* and *ii* in *Center* both have Φ = 14%, with smallest (D_p = 15 nm) and largest (D_p = 28 nm) particles, respectively; *Left* and *Right* have D_p = 15 nm. (Scale bars, 1 μm.) (*C*) Average aggregate sizes (R_{agg}) and (*D*) specific surface area (S_{spe}) of the four samples in *B* from image analysis. Error bars are SEM from at least 4,000 aggregates from each nanocomposite. *$P < 0.05$ of R_{agg} and S_{spe} (one-way ANOVA with Tukey's tests).

reduces the influence of aggregate outliers with very low abundance on R_{agg}.

Fig. 1*C* shows values for R_{agg} of each composite. With D_p = 15 nm, R_{agg} = 20 ± 3 nm (mean ± SEM) for Φ = 14% and 22.5% and R_{agg} increases slightly to 23.5 ± 3 nm for Φ = 3%. At Φ = 14% and D_p = 28 nm, R_{agg} = 59 ± 8.5 nm. A straightforward metric to evaluate Φ and R_{agg} simultaneously is the specific surface area ($S_{spe} = \Phi/R_{agg}$) (Fig. 1*D*). Interestingly, samples with low concentrations of small particles (Φ = 3%, D_p = 15 nm) and higher concentrations of large particles (Φ = 14% D_p = 28 nm) resulted in composites with similar S_{spe}. Therefore, this sample set allows us to independently investigate the impact of filler volume fraction and filler size on the strain-hardening behavior of real industrial nanomaterials.

Nanocomposite strain hardening under tensile loads. We quantified the effect of filler size and Φ on strain hardening of the nanocomposites using tensile tests. True stress (σ_{True})–extension ratio (λ) curves. curves of NBR composites, are shown in Fig. 2*A*. Engineering stress (σ_{eng}) and strain (ε_{eng}) curves are shown as *SI Appendix*, Fig. S3, for reference (see *Materials and Methods* for relation among ε_{eng} and λ as well as σ_{True} and σ_{eng}). The curves in Fig. 2*A* end abruptly because of composite fracture. All composites showed strain hardening (increase in slope) at large strains (and showed no evidence of necking—no clear Consideré tangents). Immediately obvious from Fig. 2*A* is the increased strain hardening at lower strain levels for increasing Φ. Interestingly, the curves with both sizes of fillers with Φ =14% appear indistinguishable. Moreover, the curves for neat NBR and for the composite with Φ = 3% also closely overlay.

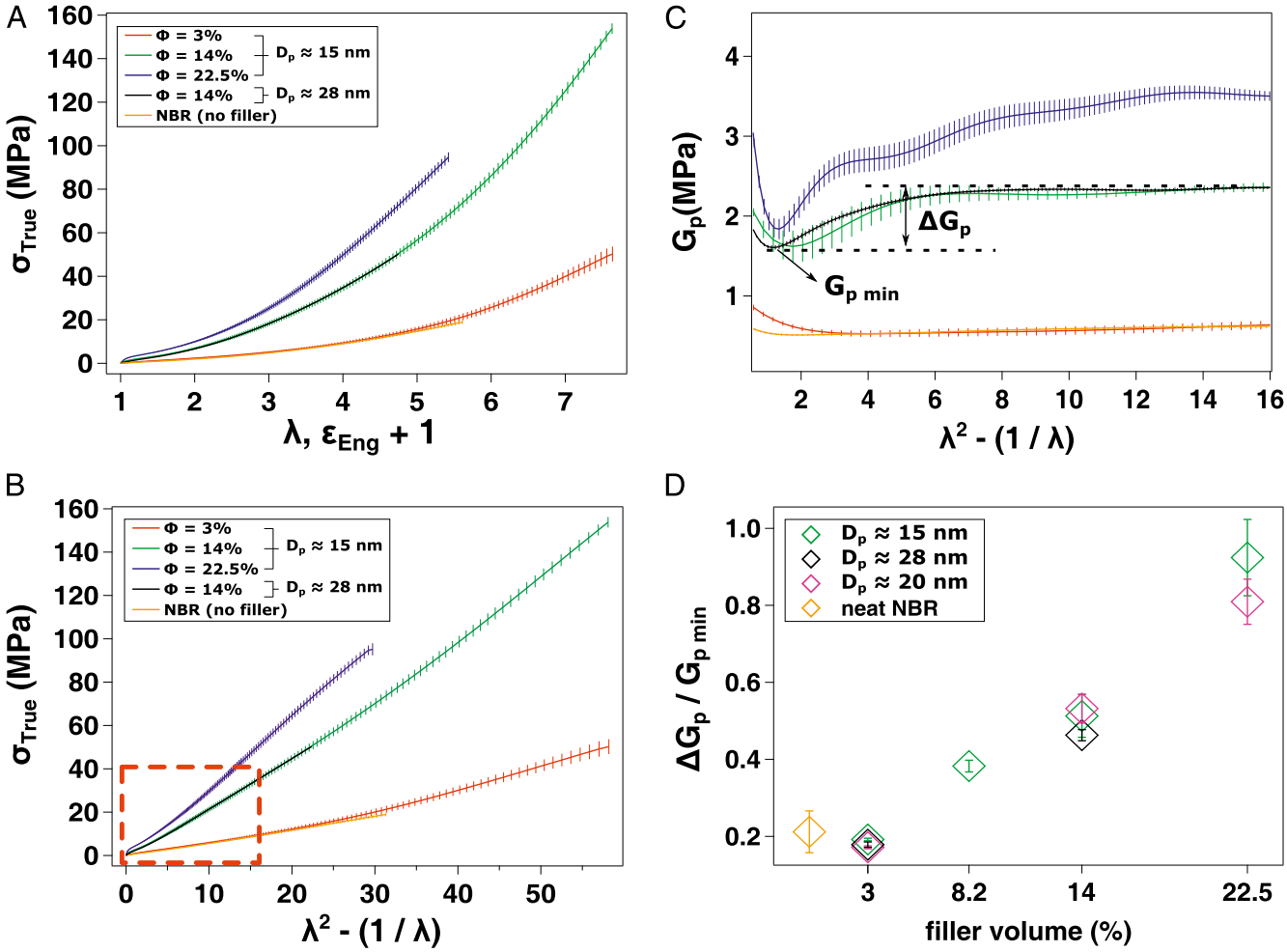

Fig. 2. Strain-hardening characteristics of nanocomposites. (*A*) True stress (σ_{True})–extension ratio (λ) curves. curves of SiO_2/NBR nanocomposites with different filler volume and size; σ_{True}–λ of the unfilled (vulcanized) NBR is shown by the orange curve. (*B*) Gaussian plots of σ_{True} versus ($\lambda^2 - 1/\lambda$) for all of the NBR systems. (*C*) Differentiation of the boxed region in the Gaussian plot shown in *B* presenting the local G_p of each sample between $\varepsilon_{eng} = 0$ and 2.9. (*D*) $\Delta G_p/G_{p,min}$ derived from Gaussian plots of many NBR nanocomposites containing different Φ and D_p of fillers. Error bars are SD of three independent measurements of three slices from the same composite slab.

To quantify the strain hardening for the data presented in Fig. 2*A*, we replotted the data in so-called Gaussian plots, which explicitly accounts for changes in sample dimensions by assuming conservation of volume during deformation. Fig. 2*B* shows Gaussian (or neo-Hookean) plots of each NBR system until their fracture points. Because each of the composites fractured at different strain, we focus on the region from $\varepsilon_{eng} = 0$–2.9 (0 to 14.95 in the Gaussian plots), as this is the maximum strain all composites could sustain (Fig. 2*B*, red box). From the plots in Fig. 2*B*, one can extract a neo-Hookean modulus, G_p. This modulus, also known as the Gaussian modulus derived by Mooney (27), was used by Hawards (28) to model cross-linked polymer composite networks as a rubbery spring in parallel with a Eyring dashpot (fillers), and another Hookean spring (fillers) (13, 14, 29–31). In this model, randomly cross-linked (vulcanized) NBR chains create a network made up of Gaussian chains (5, 21, 22),

$$\sigma_{True} = G_p\left(\lambda^2 - \frac{1}{\lambda}\right),$$

where $\lambda = \varepsilon_{eng} + 1$ and G_p is the neo-Hookean modulus. This relation allows one to quantify the elasticity of the material, even at high strains, because of the scaling of $[\lambda^2 - (1/\lambda)]$. Differentiating the Gaussian plot $\{d\sigma_{True}/d[\lambda^2 - (1/\lambda)]\}$ allows comparison of G_p as function of strain to quantify the increase in elasticity of the samples. We quantify the strain hardening of the materials by calculating the percent increase in G_p between its minimum value $G_{p,\min}$ at early strains and value at $[\lambda^2 - 1/\lambda] = 14.95$ ($G_{p,\max}$), $\Delta G_p/G_{p,min}$. Consistent with data in Fig. 2*B*, $\Delta G_p/G_{p,min}$ is statistically identical for both samples with $\Phi = 14\%$ and for neat NBR and $\Phi = 3\%$. Fig. 2*D* further shows the trend that $\Delta G_p/G_{p,min}$ increases with Φ, independent of filler size, for a variety of NBR nanocomposite formulations. Statistical testing of $\Delta G_p/G_{p,min}$ in many different NBR samples confirmed the finding that strain hardening varied only with Φ and was independent of filler size (*SI Appendix*, Fig. S4), which is contrary to reinforcement in the same samples (23).

In situ chain alignment during nanocomposite uniaxial stretching. We used in situ vibrational spectroscopy to measure molecular chain alignment during uniaxial tension application using polarized Raman microspectroscopy. In our measurements, the sample was rotated such that the Raman excitation laser was polarized parallel or perpendicular to the loading direction at each strain level (ε_{eng}), and all Raman scattered light was detected; there was no polarizer in front of the detector, as we were uninterested in depolarization ratios. Raman spectra at each ε_{eng} were recorded as $A_{\parallel}$ or $A_{\perp}$, depending on whether the laser polarization was parallel

or perpendicular, respectively, to the stretching direction. We calculated the $\langle P_2 \rangle$ coefficient from these amplitudes and refer to this coefficient as the molecular order parameter, $S_{mol} = (A_{\parallel} - A_{\perp})/(A_{\parallel} + 2A_{\perp})$ (18, 32). S_{mol} is zero for a perfectly isotropic vibration. For a perfectly anisotropic vibrational mode of a molecular group aligned parallel or orthogonal to the loading direction, S_{mol} is 1 or −0.5, respectively. In the case of stretching vibrations, such as the C≡N or C=C stretches, the Raman signal probes nuclear motion along the bond axis, so S_{mol} reflects bond orientation.

An important challenge of polarized Raman measurements is spectral normalization to account for spatial heterogeneity from different positions and for intersample comparison. This is critical for obtaining an accurate measurement of S_{mol} and comparing measurements within and among nanocomposites. We verified that it was possible to use vibrational modes that exhibit no anisotropy as normalizing vibrations with measurements in amorphous polystyrene as a reference. Our results for anisotropy in polystyrene after normalizing background-subtracted spectra by the CH_3 rocking vibration (1,033 cm^{-1}) corresponded very well with previous studies using infrared dichroism (*SI Appendix*, Fig. S5) (33–36). Therefore, we used a similar normalization protocol for NBR samples. We observed that the CH_2 twisting (tw) vibration (1,300 cm^{-1}) showed no anisotropy in strained NBR spectra, and thus the CH_2 tw peak was used as an independent peak for normalization of $A_{\parallel}$ and $A_{\perp}$ in all NBR spectra.

We focus on the C=C stretch (1,666 cm^{-1}) from the *trans*-1,4-butadiene monomer (marked by letter "k" in Fig. 3*A*) (37, 38) and C≡N stretch (2,235 cm^{-1}) vibrations in NBR to quantify

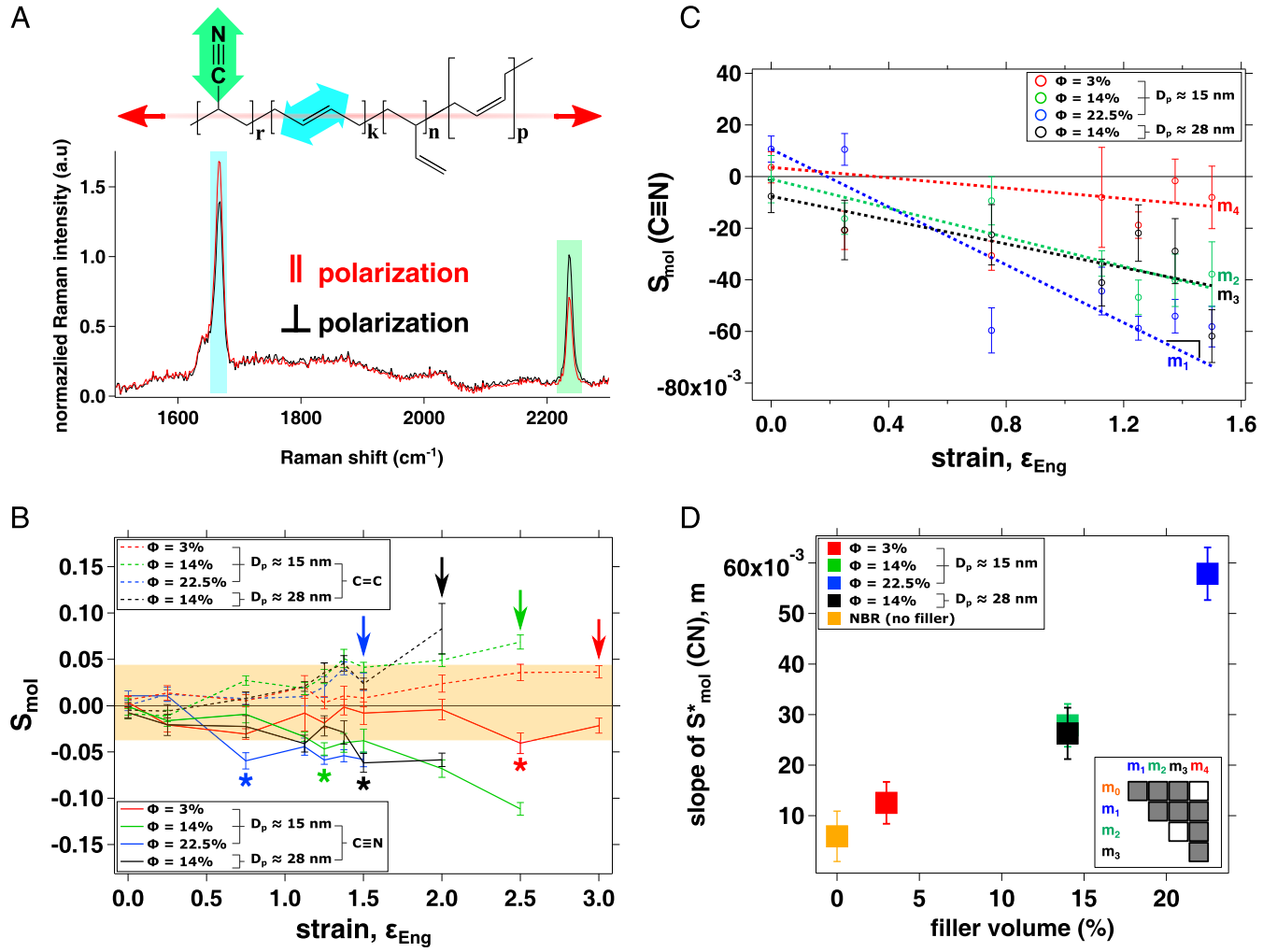

Fig. 3. Polymer anisotropy and molecular spectroscopy of uniaxially stretched nanocomposites. (*A*) Molecular structure of an NBR chain aligned to the stretching direction (red line with arrows). Letters r, k, n, and p represent different monomer units in NBR (*Materials and Methods*). Cyan and green double-sided arrows highlight the direction of the C=C (from *trans*-1,4-butadiene) and C≡N stretching vibrations, respectively. Raman peaks corresponding to these vibrations are highlighted in the example Raman spectra of a stretched (ε_{Eng} = 2.5) nanocomposite (Φ = 14%, D_p = 15 nm). The red and black lines show spectra obtained when the Raman excitation light was parallel and perpendicular, respectively, to the loading direction. (*B*) Molecular anisotropy (S_{mol}) at increasing strains (ε_{eng}) in different nanocomposites with different amount and D_p fillers. S_{mol} (C=C) from *trans*-1,4-butadiene (1,665 cm^{-1}) and S_{mol} (C≡N) (2,235 cm^{-1}) stretching vibrations are shown with dashed and straight lines, respectively. Top and bottom orange boxes show the maximum SEM of S_{mol} (C=C, top) and minimum SEM of S_{mol} (C≡N, bottom) from the neat NBR data. Asterisks indicate critical ε_{eng} levels where the significant anisotropies ($P < 0.05$) were observed compared with unstrained samples (ε_{eng} = 0) (one-way ANOVA with Tukey's and Student Newman–Keuls tests). Colored arrows show the largest bearable ε_{eng} before fracture. (*C*) Linear fits to the S_{mol} (C≡N) between ε_{eng} levels of 0 and 1.5. The slope (*m*) of NBR without any filler inside (m_0) is shown in *SI Appendix*, Fig. S8. Error bars in *B* and *C* are SEM from a minimum of six spectra (each for $A_{\parallel}$ and $A_{\perp}$ at each ε_{Eng}) from different locations from at least three different slices of each nanocomposite. (*D*) Relation between the slope values and filler amount. (*Inset*) Statistical differences of each pair of slopes ($P < 0.05$, *t* test) in a box chart are shown by gray boxes. Error bars are SD from the regression line fits presented in *C*.

anisotropy and chain alignment. The C=C backbone and C≡N sidechain group will align (somewhat) parallel and perpendicular, respectively, to the loading direction as chain alignment increases (Fig. 3*A* and *SI Appendix*, Fig. S6). Fig. 3*B* shows S_{mol} for both vibrations. As expected, we find that S_{mol} (C=C) became more positive and S_{mol} (C≡N) became more negative with increasing ε_{eng} for all nanocomposite samples. The top and bottom halves of the box in Fig. 3*B* mark the maximum SEM in S_{mol} (C=C) and S_{mol} (C≡N), respectively, from the measurements of the unfilled (but vulcanized) NBR, which never showed a statistically significant S_{mol} value at any ε_{eng} compared with the S_{mol} ($\varepsilon_{eng} = 0\%$).

In the subsequent quantification and discussion of anisotropy, we restrict our attention to the C≡N sidechain group because it is a more sensitive marker of chain alignment. This choice is substantiated by the following reasons. First, from a geometrical standpoint, a fully stretched NBR chain (Fig. 3*A*) will never show purely unidirectional C=C polarizability along the bond of the *trans*-1,4-butadiene because, by definition, this bond cannot align perfectly to the loading direction. Second, the bonding geometry of C≡N is necessarily orthogonal to the (C−C bonds in the) NBR backbone due to the *sp* (orbital) hybridization of the carbon atom. Therefore, the alignment axes of the polymer backbone and C≡N stretching polarizability are nearly orthogonal, which will increase the anisotropy of this group compared with the C=C bond when a chain is aligned. Consistent with these arguments, we experimentally observed more S_{mol} (C≡N) data points appearing outside of the orange box compared with S_{mol} (C=C). We note that, in addition to the C≡N sidechain, a similarly negative anisotropy was observed for CH_2 groups for the CH_2 symmetric vibration (2,846 cm^{-1}), which should also lie orthogonal to the chain backbone (*SI Appendix*, Fig. S7*A*). Taken together, this underscores the robustness of our measurement protocol and molecular anisotropy measurements.

In Fig. 3*B*, asterisks mark the critical ε_{eng}, defined as the ε_{eng} at which we first observed a statistically significant ($P < 0.05$) increase in S_{mol} (C≡N) compared with S_{mol} (C≡N) at $\varepsilon_{eng} = 0$ for each sample. The most prominent trend observed in Fig. 3*B* is that the critical ε_{eng} required to develop a statistically significant C≡N vibrational anisotropy decreased with increasing Φ. We conclude that adding more fillers (increasing Φ) causes NBR chains to align to a greater extent for a given deformation. For the two nanocomposites with Φ = 14%, we observed a critical ε_{eng} that was slightly lower for the composite with smaller R_{agg} (Fig. 3*B*, green) compared to that with increased R_{agg} (Fig. 3*B*, black); otherwise, the S_{mol} (C≡N) vs. ε_{eng} traces for these materials look extremely similar.

As a method to compare the trends in Fig. 3*B*, we linearly fit the S_{mol} (C≡N) vs. ε_{eng} for each composite from $\varepsilon_{eng} = 0$ until $\varepsilon_{eng} = 1.5$ (Fig. 3*C*). This range was chosen because $\varepsilon_{eng} = 1.5$ was the highest ε_{eng} from which we were able to collect Raman data from all samples. The slope of each fit, $m = (\Delta S_{mol})/(\Delta\varepsilon_{eng})$, is a measure for how increasing ε_{eng} induces C≡N anisotropy, and therefore chain alignment, in the composites. Fig. 3*D* shows that *m* increases with Φ, and the results from statistical comparison of *m* from different samples are summarized in *Inset*; significant differences between two slopes ($P < 0.05$) are shown by gray boxes. All slopes were statistically independent except for those from the composites with Φ = 14%, which again confirms that volume fraction, but not filler size, affects chain alignment.

Because the slope in anisotropy, *m*, and $\Delta G_p/G_{p,min}$ both vary with Φ, we plotted these variables against one another in Fig. 4. This graph clearly shows that these variables are positively correlated, indicating that strain hardening can be predicted by chain alignment and vice versa for our nanocomposites. Previous work has shown that filler size strongly affects reinforcement in elastomers (12, 23) and strain hardening in semicrystalline composites (8); it is therefore surprising that filler size has almost no effect on chain alignment or strain hardening.

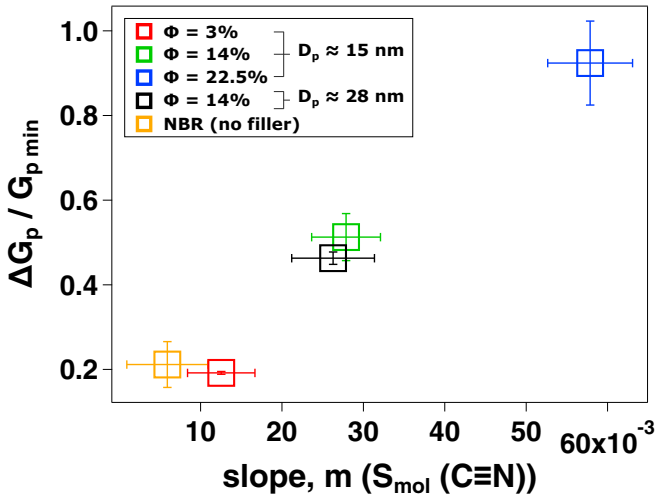

Fig. 4. Correlation between strain hardening and chain anisotropy in nanocomposites. Graph shows relation between the $|m|$ from the chain alignment measurements (Fig. 3*D*) and the strain hardening ($\Delta G_p/G_{p,min}$, Fig. 2*D*) of all samples. Error bars of $\Delta G_p/G_{p,min}$ are SD ($n = 3$) and slopes, *m*, are SD obtained from the linear regression line fits.

Modeling Chain Anisotropy in Strained Nanocomposites. To further interpret the chain alignment experiments, we developed a model for how chain alignment develops under strain and is affected by filler properties. As a starting point, we consider three types of NBR chains in a nanocomposite (Fig. 5*A*): type 1 chains that are wrapped around (bound to) the fillers, type 2 chains that exist within the polymer bulk and not in the vicinity of fillers, and type 3 chains that exist within space between two fillers—referred to as "bridging" chains. Type 1 chains will necessarily have C≡N side groups that are radially symmetric and will therefore not contribute to S_{mol} (C≡N). From our measurements in unfilled, vulcanized NBR, we empirically found that type 2 chains generate no detectable anisotropy of C≡N bonds (*SI Appendix*, Fig. S8). This leaves type 3 bridging chains as the primary contributor to the measured C≡N anisotropy, which is certainly plausible based on previous work suggesting how fillers act to trap entanglements between which bridging chains can undergo strain stiffening (3, 39).

We assume that each type 3 chain contributes a certain amount of Raman signal to $A_\perp$ and $A_\parallel$—the C≡N vibration Raman intensities acquired orthogonal and parallel to the loading direction—such that $1 = A_\parallel + A_\perp$. In the simplest meaningful assumption that each neat NBR chain has *N* monomers, each with a size *a*, we can write $A_\perp \approx [(L - R_p)/(2Na)] + 0.5$, where *L* parameterizes the space between fillers and R_p is the end-to-end distance of a neat NBR chain in the melt. This relation states that the Raman amplitude for C≡N vibrations in a type 3 chain in the direction orthogonal to the loading direction scales proportionally with distance between fillers and inversely with chain contour length, which follows intuition for bridging chains. In addition, when $L = R_p$, the chain is essentially in a relaxed coil configuration, so there is no preferential orientation of C≡N bonds, and $A_\parallel = A_\perp = 0.5$, meaning that $S_{mol} = 0$. We note that this relation uses the contour length *Na* as the comparison instead of the chain end-to-end distance because the contour length is the relevant distance for comparison when discussing strain stiffening and anisotropy of chains; a straight chain will be maximally anisotropic.

The space between fillers $L \approx L_o(1 + \varepsilon_{eng})$, where L_0 is the space between fillers in the unstrained composite, and we assume affine deformation. A schematic for the model is shown in Fig. 5*A*. We derived L_0 in two ways for the NBR composites: (*i*) from the TEM images by calculating the average distance between each

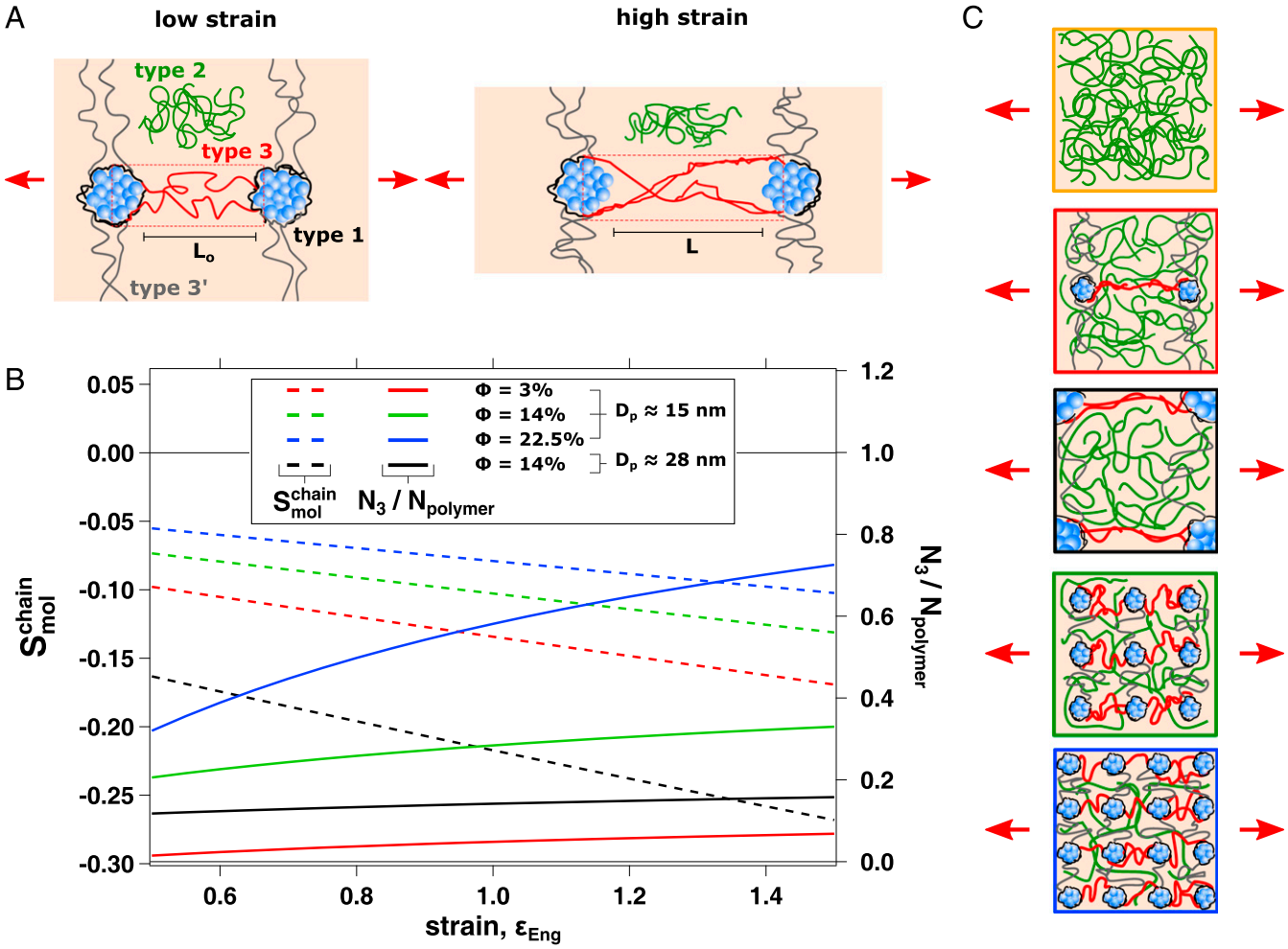

Fig. 5. Modeling chain alignment in nanocomposites. (*A*) Illustration showing the three different types of NBR chains in a typical nanocomposite for our scaling theory at low strain (*Left*) and high strain (*Right*). Type 1 (black) and type 2 (green) chains represent filler-adsorbed and bulk rubber, respectively. Type 3 (red) chains bridge the filler aggregates to each other and are called bridging chains. Type 3′ (gray) chains are bridging chains in the direction orthogonal to the load, which are not considered here. The bridging region is indicated by the red box with dashed lines. Under strain, type 1 chains can delaminate from particles, enter the bridging region, and convert to type 3 chains. (*B*) Graph showing calculated S_{mol}^{chain} (C≡N bonds, dashed lines) and fractional number of type 3 chains ($N_3/N_{polymer}$, solid lines) as a function of ε_{eng} based on the scaling argument presented in the *Modeling Chain Anisotropy in Strained Nanocomposites*. S_{mol}^{chain} decreases (becomes more negative) and $N_3/N_{polymer}$ increases with ε_{eng}. (*C*) Schematic illustrations of the predicted ultrastructural features in nanocomposites at ε_{eng} = 1.5. Ultrastructure of neat NBR is illustrated in the orange box. Microstructures sketched in red, green, and blue boxes represent the composites including small fillers (D_p ~ 15 nm) at Φ = 3%, 14%, and 22.5%, respectively. Microstructure in black is for Φ = 14% with the larger filler particles (D_p ~ 28 nm). Color codes of different types of polymer chains are the same as those in *A*. The L_o and R_{agg} represented in each illustration are scaled realistically, under the assumption that aggregates are Dirac-distributed in a cubic lattice.

aggregate and its four nearest neighbors (because we had 2D TEM images) and fitting histograms with Gaussians (*SI Appendix*, Fig. S9) and (*ii*) by calculating L_0 using a conservation of volume argument $L_0 \approx R_{agg}[(1-\Phi)/\Phi]^{1/3}$, where Φ is volume fraction and R_{agg} is the characteristic filler (aggregate) radius from Fig. 1. Although the exact numbers from the two methods are different (see *SI Appendix*, Fig. S10), the trends for these independent measurements of L_0 are nearly identical, showing that assuming a narrow or Dirac delta distribution of L_0 is, in fact, a reasonable approximation for polydisperse nanocomposites. In our model calculations, we use the numbers extracted from the TEM for L_0 and note that, although the composites were polydisperse, all materials showed a clear peak in the L_0 histograms, indicating that, for predicting average quantities, as we do for S_{mol}, the fitted mean L_0 from the histograms is appropriate. Therefore, we performed all subsequent calculations for Fig. 5 with the mean L_0.

With this model defined, it is possible to calculate S_{mol} as we measure it in the experiment by assuming a fractional contribution to S_{mol} from type 1, type 2, and type 3 chains weighted by the fractional amount of each type of chain ($N_x/N_{polymer}$), where N_x is the number of type 1, 2, or 3 chains and $N_{polymer}$ is the total number of chains in the focal volume of the Raman measurement. We know, from experiment, that type 1 and type 2 chains contribute virtually nothing to S_{mol}, and it is possible to calculate S_{mol} from a single type 3 chain (S_{mol}^{chain}) based on the $A_\perp$ and $A_\parallel$ for that chain. By multiplying this value by the fractional amount of type 3 chains, $N_3/N_{polymer}$, in the focal volume, we arrive at the total S_{mol} value, which has the form

$$S_{mol} = \frac{N_3}{N_{polymer}} S_{mol}^{chain} = \frac{N_3}{N_{polymer}} \left\{ \frac{1 - 2\left[\frac{\frac{L_0(1+\varepsilon_{eng}) - R_p}{2}}{Na} + 0.5\right]}{1 + \left[\frac{\frac{L_0(1+\varepsilon_{eng}) - R_p}{2}}{Na} + 0.5\right]} \right\}. \quad [1]$$

From our measured L_0 and fitted lines in Fig. 3*C*, we calculated $N_3/N_{polymer}$ and S_{mol}^{chain} as function of ε_{eng}, assuming $Na \approx 1{,}000$ nm for an NBR chain with a molecular weight of 2.5×10^5 g/mol and

$R_p \approx 30$ nm (22). There are no other free parameters in this calculation. This model allows us to investigate the mechanism of increasing S_{mol} (C≡N) with ε_{eng} for the different composites with respect to individual chain anisotropy and fractional amount of contributing type 3 chains.

Our calculations showed that $N_3/N_{polymer}$ and $|S_{mol}^{chain}|$ increase with ε_{eng} for all systems and that $N_3/N_{polymer}$ was largest at largest Φ whereas $|S_{mol}^{chain}|$ was smallest at largest Φ (Fig. 5*B*). Interestingly, at $\Phi = 14\%$, we observed that $N_3/N_{polymer}$ was larger with smaller R_{agg} (because there are comparatively more bridging chains for greater S_{spe}), whereas $|S_{mol}^{chain}|$ was larger with larger R_{agg} (because of the larger L_0 between aggregates). Because the total S_{mol} is proportional to $(N_3/N_{polymer}) \cdot S_{mol}^{chain}$, this model reveals that the two terms of this product appear to compensate one another.

Fig. 5*C* shows nanocomposite ultrastructures at $\varepsilon_{eng} = 1.5$ based on our model and experimental chain alignment data. Unfilled NBR (orange box, Fig. 5*C*) only has type 2 (green) chains due to the absence of fillers. Weak anisotropy could, in principle, originate from type 2 chains, but this was undetectable in our spectroscopic measurements. In the presence of the lowest volume fraction fillers ($\Phi = 3\%$), type 3 (red) chains begin to weakly contribute to the measured S_{mol}. Because Φ is relatively low, the fractional amount of bridging chains is quite low, whereas the anisotropy of type 3 bridging chains ($|S_{mol}^{chain}|$) is quite large because L_0 is large. The effect of small initial $N_3/N_{polymer}$ makes S_{mol} (C≡N) detectable only at large strains where $|S_{mol}^{chain}|$ increases and the fractional amount of type 3 chains also increases.

Samples with $\Phi = 14\%$ are shown in the black and green boxes in Fig. 5*C* for the samples with large and small R_{agg}, respectively. Larger R_{agg} increases L_o, leading to larger $|S_{mol}^{chain}|$. However, the nanocomposite with smaller R_{agg} has smaller L_o and larger S_{spe}, which increases the number of the bridging chains ($N_3/N_{polymer}$) in the same volume relative to the sample with larger R_{agg}. These two effects cancel out, resulting in the same S_{mol} for both samples. When $\Phi = 22.5\%$ (blue box in Fig. 5*C*), L_o and $|S_{mol}^{chain}|$ are smallest of all measured nanocomposites, but $N_3/N_{polymer}$ is largest because the aggregates are most densely packed (and have the largest S_{spe}), leading to the largest measured chain alignment.

Importantly, we compared the fractional amount of type 3 bridging chains $N_3/N_{polymer}$ predicted based on the anisotropy model with that from a scaling argument based on the geometry and filler properties of each nanocomposite (see *SI Appendix* for a detailed description). The calculations of $N_3/N_{polymer}$ from the scaling argument compare favorably with the predictions from our anisotropy model, in that both show a similar trend with volume fraction and aggregate size (see *SI Appendix*, Fig. S16). The fractional amount of bridging chains shows the following order in both the anisotropy model (Fig. 5) and our geometrical scaling argument: $N_3/N_{polymer}$ ($\Phi = 22.5\%$, $D_p = 15$ nm) > $N_3/N_{polymer}$ ($\Phi = 14\%$, $D_p = 15$ nm) > $N_3/N_{polymer}$ ($\Phi = 14\%$, $D_p = 28$ nm) > $N_3/N_{polymer}$ ($\Phi = 3\%$, $D_p = 15$ nm). Given that our scaling argument employs a Dirac delta distribution for the filler aggregate size and does not account for conversion of type 1→type 3 chains, the general agreement between these two independent approaches supports the idea that the fractional amount of type 3 chains codetermines the molecular anisotropy in nanocomposites.

Having derived a relation for $N_3/N_{polymer}$ in *SI Appendix*, Eq. **S1** and recalling the equation for S_{mol} from Eq. **1**, we can verify if S_{mol} is indeed independent of R_{agg}. From *SI Appendix*, Eq. **S1**, we can write the dependence of $N_3/N_{polymer}$ with R_{agg} as

$$\frac{N_3}{N_{polymer}} \sim \frac{1}{R_{agg}}. \quad [2]$$

By graphing the term in brackets in Eq. **1** (S_{mol}^{chain} for bridging chains) and substituting $L_0 \approx R_{agg}[(1-\Phi)/\Phi]^{1/3}$, we empirically found that

$$S_{mol}^{chain} \approx R_{agg}^{x}, \quad [3]$$

where $0.90 < x < 0.97$, depending on volume fraction ($\Phi = 0.03$–0.225) and applied strain ($\varepsilon_{eng} = 0$–1.2) between 10 nm < R_{agg} < 100 nm. Multiplying Eqs. **2** and **3** quantitatively predicts that S_{mol} is essentially independent of R_{agg} and that the fractional amount of bridging chains and molecular anisotropy of a single chain compensate one another with regard to changes in R_{agg}.

Relation Between Nancomposite Anisotropy and Strain Hardening. Our work shows how strain hardening and strain-induced chain alignment are strongly correlated and vary with Φ alone, independent of nanofiller ultrastructure. Within the context of our model, the mechanism underlying how increasing ε_{eng} increases $|S_{mol}^{chain}|$ and $N_3/N_{polymer}$, thereby increasing S_{mol}, follows the forthcoming logic. (*i*) L increases with strain, increasing $|S_{mol}^{chain}|$ for bridging chains until it reaches a maximum (−0.5), and (*ii*) type 1 chains are converted to type 3 chains via shear-induced (or tension-induced) delamination of type 1 chains from the filler surface (Fig. 5*A*, red dotted boxes). We note that the thickness of the so-called bound layer (type 1 chains) increases with aggregate size (*SI Appendix*, Fig. S11), similar to previous work (40, 41), which could also enhance the bridging effect—increase $N_3/N_{polymer}$—by increasing the effective bridging region volume relative to the total volume of the composite (42); however, the precise effect of boundary layer thickness on the different composite systems is not clear. Conversion of "slippery" adsorbed (type 1) chains into type 3 chains has been shown, specifically in samples (nearly identical to ours) where limited interaction between the polymer and fillers is present (19, 43). As noted in *SI Appendix*, Fig. S1, van der Waals forces are the primary mechanism of adhesion between the NBR and filler aggregates, and this results in a substantially weaker bound polymer layer to the silica compared with either covalent or hydrogen bound polymers (see *SI Appendix*). This finding supports the idea that applied tension could delaminate NBR chains from silica surfaces. Importantly, even if NBR chains are weakly adhered in a bound layer to silica, previous work has shown that even minimal adhesion permits substantial strain stiffening (and therefore anisotropy development) in bridging chains between aggregates (39, 44). Although it is, in principle, possible to disrupt filler aggregates with increasing tensile strain, which would have a similar effect as delamination—that is creating more (type 3) bridging chains—scanning electron micrograph images of 150% strained nanocomposite samples show no such effects (*SI Appendix*, Fig. S12).

Recalling again the results of Jancar et al. (8) where PMMA microcomposites showed almost no strain hardening compared with nanocomposites at the same Φ, this raises an interesting question. Over what length scale do type 3 chains exist, and therefore contribute tangible chain alignment, in composite systems? Looking at our data from unfilled and $\Phi = 3\%$ nanocomposites, we conjecture that detectable chain alignment only occurs when L_o is on the order of R_p of the neat NBR chain because, although a large L_0 (>> R_p) would lead to large $|S_{mol}^{chain}|$, it will also result in a vanishing amount of $N_3/N_{polymer}$. In microcomposites, L_o is approximately micrometers (>>R_p of the PMMA), whereas L_o is comparable to R_p in nanocomposites. Therefore, the microcomposite case approaches that of a vanishingly low Φ (and $N_3/N_{polymer}$) in nanocomposites, where almost no type 3 chains exist, which results in minimal overall chain alignment and therefore minimal strain hardening.

Conclusion

The effect of nanofiller size and amount on nonlinear strain hardening of cross-linked elastomers ($T_g \approx -30$ °C) was quantified here for various NBR nanocomposites. By measuring both their mechanical strain hardening and chain alignment with

increasing tensile strain, we show that both quantities in NBR composites only depend on filler amount and were independent of the filler size. Furthermore, these two variables were positively correlated, highlighting the relation between them. Using scaling arguments, we arrive at a mechanism for chain alignment that only depends on filler volume fraction via a compensatory effect between individual chain alignment and number of (bridging) chains aligning to the load. Although our work highlights the importance of chains bridging filler aggregates over a length scale comparable with the end-to-end distance of a chain, Baeza et al. (45) recently related the linear elasticity in nanocomposites to network formation among overlapping tightly bound chains in close proximity (approximately angstroms to nanometers) to filler surfaces. Along with our results showing that nonlinear elasticity of nanocomposites is insensitive to filler size, the longer length scale we identify underscores the different physicochemical origin of the linear and nonlinear elasticity in these materials. This different origin suggests that nanocomposite design can be optimized in a two-tiered process wherein one tunes the strain hardening properties and mechanical reinforcement independently by (*i*) choosing an amount of nanofillers to target a specific nonlinear strain hardening response and (*ii*) selecting a particular size of nanofillers to obtain a desired reinforcement.

Materials and Methods

SiO_2 [primary particle sizes (diameters), D_p are *ca*. 15 nm, 20 nm, and 28 nm]/NBR (M_w = 250,000 g/mol, glass transition temperature, $T_g \approx -36$ °C; see *SI Appendix*, Fig. S13) nanocomposites were produced at SKF Elgin (46). In terms of per hundred rubber units (PHR), the filler amounts in the NBR composites can be rewritten as 10 PHR (Φ = 3%), 30 PHR (Φ = 8.2%), 50 PHR (Φ = 14%), and 90 PHR (Φ = 22.5%). Other fundamental ingredients and their amounts in all NBR systems are NBR (100 PHR), stearic acid (1 PHR), ZnO (9 PHR), rubber activator (2.5 PHR), sulfur (1.2 PHR), and curing agent (2.5 PHR). Other than the volume and D_p of the fillers, all other synthetic parameters were kept the same. Unfortunately, further mixing and synthetic details of the NBR composites cannot be provided here. Briefly, NBR rubber synthesized as nitrile elastomers, which are synthesized via emulsion polymerization of 1,3-butadiene and acrylonitrile with the monomer ratio of 72:28. Detailed experimental methods can be found in *SI Appendix*.

ACKNOWLEDGMENTS. We acknowledge Florian Gericke, Walter Scholdei, Jürgen Worm, and Marc-Jan van Zadel for excellent technical support with building the spectroscopy setup. Andreas Hanewald and Sabine Pütz assisted with measurements of strain hardening and T_g, respectively. We thank Tristan Bereau, Frederik Fleissner, Johannes Hunger, and Kurt Kremer for stimulating discussions, and William Rock helped with analytical software development. This work is part of the research programme "Understanding the viscoelasticity of elastomer based nanocomposites" of the Stichting voor Fundamenteel Onderzoek der Materie, which is financially supported by the Nederlandse Organisatie voor Wetenschappelijk Onderzoek.

1. Carey BJ, Patra PK, Ci L, Silva GG, Ajayan PM (2011) Observation of dynamic strain hardening in polymer nanocomposites. *ACS Nano* 5:2715–2722.
2. Huang Y, Paul DR (2007) Effect of molecular weight and temperature on physical aging of thin glassy poly(2,6-dimethyl-1,4-phenylene oxide) films. *J Polym Sci, B, Polym Phys* 45:1390–1398.
3. Jancar J, et al. (2010) Current issues in research on structure–property relationships in polymer nanocomposites. *Polymer* 51:3321–3343.
4. Fried JR (2003) *Polymer Science and Technology* (Prentice Hall, Englewood Cliffs, NJ).
5. Riande E, Diaz-Calledja R, Prolongo MG, Masegosa RM, Salom C (2000) *Polymer Viscoelasticity: Stress and Strain in Practice* (Marcel Dekker, New York).
6. Haward RN (1993) Strain hardening of thermoplastics. *Macromolecules* 26:5860–5869.
7. Na B, et al. (2007) Inverse temperature dependence of strain hardening in ultrahigh molecular weight polyethylene: Role of lamellar coupling and entanglement density. *J Phys Chem B* 111:13206–13210.
8. Jancar J, Hoy RS, Lesser AJ, Jancarova E, Zidek J (2013) Effect of particle size, temperature, and deformation rate on the plastic flow and strain hardening response of PMMA composites. *Macromolecules* 46:9409–9426.
9. Pukanszky B (1990) Influence of interface interaction on the ultimate tensile properties of polymer composites. *Composites* 21:255–262.
10. Costa P, et al. (2012) Mechanical, electrical and electro-mechanical properties of thermoplastic elastomer styrene–butadiene–styrene/multiwall carbon nanotubes composites. *J Mater Sci* 48:1172–1179.
11. Riggleman RA, Toepperwein G, Papakonstantopoulos GJ, Barrat J-L, de Pablo JJ (2009) Entanglement network in nanoparticle reinforced polymers. *J Chem Phys* 130:244903.
12. Sternstein SS, Zhu AJ (2002) Reinforcement mechanism of nanofilled polymer melts as elucidated by nonlinear viscoelastic behavior. *Macromolecules* 35:7262–7273.
13. Jiang F, et al. (2015) Combination of magnetic and enhanced mechanical properties for copolymer-grafted magnetite composite thermoplastic elastomers. *ACS Appl Mater Interfaces* 7:10563–10575.
14. Jiang F, Zhang Y, Fang C, Wang Z, Wang Z (2014) From soft to strong elastomers: The role of additional crosslinkings in copolymer-grafted multiwalled carbon nanotube composite thermoplastic elastomers. *RSC Advances* 4:60079–60085.
15. Pei A, Malho JM, Ruokolainen J, Zhou Q, Berglund LA (2011) Strong nanocomposite reinforcement effects in polyurethane elastomer with low volume fraction of cellulose nanocrystals. *Macromolecules* 44:4422–4427.
16. Ha YH, Thomas EL (2002) Deformation behavior of a roll-cast layered-silicate/lamellar triblock copolymer nanocomposite. *Macromolecules* 35:4419–4428.
17. Bokobza L (2001) Filled elastomers: A new approach based on measurements of chain orientation. *Polymer* 42:5415–5423.
18. Bokobza L, et al. (2002) Effects of filler particle/elastomer distribution and interaction on composite mechanical properties. *Chem Mater* 14:162–167.
19. Wang Z, Liu J, Wu S, Wang W, Zhang L (2010) Novel percolation phenomena and mechanism of strengthening elastomers by nanofillers. *Phys Chem Chem Phys* 12:3014–3030.
20. Bistričić L, Leskovac M, Baranović G, Blagojević SL (2008) Mechanical properties and linear infrared dichroism of thin films of polyurethane nanocomposites. *J Appl Polym Sci* 108:791–803.
21. Treloar LR (1975) *The Physics of Rubber Elasticity*, ed Treloar LR (Oxford Univ Press, Oxford).
22. Rubinstein M, Colby RH (2003) *Polymer Physics* (Oxford Univ Press, Oxford).
23. Mermet-Guyennet MRB, et al. (2015) Size-dependent reinforcement of composite rubbers. *Polymer* 73:170–173.
24. Suzuki N, Ito M, Ono S (2005) Effects of rubber/filler interactions on the structural development and mechanical properties of NBR/silica composites. *J Appl Polym Sci* 95:74–81.
25. Lopez JF, Perez LD, Lopez BL (2011) Effect of silica modification on the chemical interactions in NBR-based composites. *J Appl Polym Sci* 122:2130–2138.
26. Varol HS, et al. (2015) Multiscale effects of interfacial polymer confinement in silica nanocomposites. *Macromolecules* 48:7929–7937.
27. Mooney M (1940) A theory of large elastic deformation. *J Appl Phys* 11:582–592.
28. Haward RN (1997) *The Physics of Glassy Polymers* (Springer, Dordrecht, The Netherlands), 2nd Ed.
29. Fang C, et al. (2015) Fabrication of copolymer-grafted multiwalled carbon nanotube composite thermoplastic elastomers filled with unmodified MWCNTs as additional nanofillers to significantly improve both electrical conductivity and mechanical properties. *Ind Eng Chem Res* 54:12597–12606.
30. Ward IM, Sweeney J (2012) *Mechanical Properties of Solid Polymers* (John Wiley, Chichester, UK), 3rd Ed.
31. Lin Y-H (2011) *Polymer Viscoelasticity: Basics, Molecular Theories, Experiments and Simulations* (World Sci, Singapore), 2nd Ed.
32. Richard-Lacroix M, Pellerin C (2013) Accurate new method for molecular orientation quantification using polarized Raman spectroscopy. *Macromolecules* 46:5561–5569.
33. Keplinger T, et al. (2015) A versatile strategy for grafting polymers to wood cell walls. *Acta Biomater* 11:256–263.
34. Prasertsri S, Lagarde F, Rattanasom N, Sirisinha C, Daniel P (2013) Raman spectroscopy and thermal analysis of gum and silica-filled NR/SBR blends prepared from latex system. *Polym Test* 32:852–861.
35. Prakanrat S, Phinyocheep P, Daniel P (2009) Spectroscopic investigation of polystyrene surface grafting on natural rubber. *Appl Spectrosc* 63:233–238.
36. Bruckmoser K, Resch K, Kisslinger T, Lucyshyn T (2015) Measurement of interdiffusion in polymeric materials by applying Raman spectroscopy. *Polym Test* 46:122–133.
37. Siesler HW, Holland-Moritz K (1980) *Infrared and Raman Spectroscopy of Polymers* (Marcel Dekker, New York).
38. Bower DI, Maddams MF (1992) *The Vibrational Spectroscopy of Polymers*, eds Cahn RW, Davis EA, Ward IM (Cambridge Univ Press, Cambridge, UK).
39. Zhu AJ, Sternstein SS (2003) Nonlinear viscoelasticity of nanofilled polymers: Interfaces, chain statistics and properties recovery kinetics. *Compos Sci Technol* 63:1113–1126.
40. Pliskin I, Tokita N (1972) Bound rubber in elastomers: Analysis of elastomer-filler interaction and its effect on viscosity and modulus of composite systems. *J Appl Polym Sci* 16:473–492.
41. Jouault N, et al. (2013) Bound polymer layer in nanocomposites. *ACS Macro Lett* 2:371–374.
42. Zhang Q, Archer LA (2002) Poly(ethylene oxide)/silica nanocomposites: Structure and rheology. *Langmuir* 18:10435–10442.
43. Kilian HG, Strauss M, Hamm W (1994) Universal properties in filler-loaded rubbers. *Rubber Chem Technol* 67:1–16.
44. Kalfus J, Jancar J (2007) Relaxation processes in PVAc-HA nanocomposites. *J Polym Sci B Polym Phys* 45:1380–1388.
45. Baeza GP, et al. (2016) Network dynamics in nanofilled polymers. *Nat Commun* 7:11368.
46. de Castro JG, et al. (2015) Nonmonotonic fracture behavior of polymer nanocomposites. *Appl Phys Lett* 106:221904.